



**Murdoch**  
UNIVERSITY

## MURDOCH RESEARCH REPOSITORY

*This is the author's final version of the work, as accepted for publication following peer review but without the publisher's layout or pagination.*

*The definitive version is available at*

<http://dx.doi.org/10.1016/j.electacta.2015.03.146>

**Penki, T.R., Shivakumara, S., Minakshi, M. and Munichandraiah, N. (2015) Porous flower-like  $\alpha$ -Fe<sub>2</sub>O<sub>3</sub> nanostructure: A high performance anode material for lithium-ion batteries. Electrochimica Acta, 167 . pp. 330-339.**

<http://researchrepository.murdoch.edu.au/26951/>

Copyright: © 2015 Elsevier Ltd.

It is posted here for your personal use. No further distribution is permitted.

## Accepted Manuscript

Title: Porous Flower-like  $\alpha$ -Fe<sub>2</sub>O<sub>3</sub> Nanostructure: A High Performance Anode Material for Lithium-ion Batteries

Author: Tirupathi Rao Penki S. Shivakumara M. Minakshi N. Munichandraiah

PII: S0013-4686(15)00763-X  
DOI: <http://dx.doi.org/doi:10.1016/j.electacta.2015.03.146>  
Reference: EA 24672

To appear in: *Electrochimica Acta*

Received date: 3-3-2015  
Revised date: 16-3-2015

Please cite this article as: Tirupathi Rao Penki, S.Shivakumara, M.Minakshi, N.Munichandraiah, Porous Flower-like *alpha*-Fe<sub>2</sub>O<sub>3</sub> Nanostructure: A High Performance Anode Material for Lithium-ion Batteries, *Electrochimica Acta* <http://dx.doi.org/10.1016/j.electacta.2015.03.146>

This is a PDF file of an unedited manuscript that has been accepted for publication. As a service to our customers we are providing this early version of the manuscript. The manuscript will undergo copyediting, typesetting, and review of the resulting proof before it is published in its final form. Please note that during the production process errors may be discovered which could affect the content, and all legal disclaimers that apply to the journal pertain.

# Porous Flower-like $\alpha$ -Fe<sub>2</sub>O<sub>3</sub> Nanostructure: A High Performance Anode Material for Lithium-ion Batteries

Tirupathi Rao Penki<sup>1</sup>, S. Shivakumara<sup>1</sup>, M. Minakshi<sup>2</sup> and N. Munichandraiah<sup>1\*</sup>

<sup>1</sup>Department of Inorganic and Physical Chemistry, Indian Institute of Science, Bangalore-560012, India.

<sup>2</sup>Department of Chemistry, Murdoch University, Murdoch, WA 6150, Australia.

\*Corresponding author.: *muni@ipc.iisc.ernet.in*

## Graphical abstract

## Abstract

Porous flower-like  $\alpha$ -Fe<sub>2</sub>O<sub>3</sub> nanostructures have been synthesized by ethylene glycol mediated iron alkoxide as an intermediate and studied as an anode material of Li-ion battery. The iron alkoxide precursor is heated at different temperatures from 300 to 700 °C. The  $\alpha$ -Fe<sub>2</sub>O<sub>3</sub> samples possess porosity and high surface area. There is a decrease in pore volume as well as surface area by increasing the preparation temperature. The reversible cycling properties of the  $\alpha$ -Fe<sub>2</sub>O<sub>3</sub> nanostructures have been evaluated by cyclic voltammetry, galvanostatic charge discharge cycling, and impedance spectroscopy measurements at ambient temperature. The initial discharge capacity values of 1063, 1168, 1183, 1152 and 968 mAh g<sup>-1</sup> at a specific current of 50 mA g<sup>-1</sup> are obtained for the samples prepared at 300, 420, 500, 600 and 700 °C, respectively. The samples prepared at 500 and 600 °C exhibit good

cycling performance with high rate capability. The high rate capacity is attributed to porous nature of the materials. As the iron oxides are inexpensive and environmental friendly, the  $\alpha$ - $\text{Fe}_2\text{O}_3$  has potential application as anode material for rechargeable Li batteries.

**Key words:** Porous  $\text{Fe}_2\text{O}_3$ , anode material, high discharge capacity, lithium ion battery

## 1. Introduction

Carbon has been used as the anode material for Li-ion batteries because of its high coulombic efficiency and safety [1]. However, carbon has limited storage capacity (theoretically,  $370 \text{ mAh g}^{-1}$ ) as well as rate capability. Research activities on novel electrode materials with improved performance for the next generation Li-ion batteries for high power applications such as electric vehicles have been intensive in recent years [2]. For this purpose, development of alternative anode materials with high capacity, long cycle-life, high rate capability and environmental compatibility is important. Metal oxides are intensively investigated as anode materials due to their higher specific capacities and volumetric energy densities [3-6]. Among the transition metal oxides, hematite ( $\alpha$ - $\text{Fe}_2\text{O}_3$ ) has attracted great interest due to its favorable properties, such as low cost, good stability, nontoxicity, and environmental friendly properties. It has been studied for applications in Li-ion batteries [7-10], supercapacitors [11-13], magnetic materials [14, 15], catalytic agents [16], gas sensors and so on [17, 18].

The theoretical capacity of  $\alpha$ - $\text{Fe}_2\text{O}_3$  is high at  $1007 \text{ mAh g}^{-1}$  assuming 6 Li per formula unit [7-10, 19-22]. One of the most challenging issues is to maintain its electrochemical stability during cycling. Upon lithiation/delithiation during cycling,  $\text{Fe}_2\text{O}_3$  suffers from volume changes and subsequently pulverization of particles leading to poor capacity retention and rate performance. It has been shown that the nanostructured  $\text{Fe}_2\text{O}_3$  enhances the rate performance and cycling stability [23]. Smaller particle size means shorter path length for

diffusion of  $\text{Li}^+$  lithium ion and electronic transport. Recently, the use of nanostructured  $\alpha\text{-Fe}_2\text{O}_3$  as an anode material has attracted interest [24], which is largely promoted by the synthesis of diverse  $\alpha\text{-Fe}_2\text{O}_3$  nanostructures, including nanoparticles [25], nanocubes [26] nanorods [27], nanotubes [28], and nanoflowers [29] by various routes.

The self-assembled metal oxide nanostructures have attracted great interest because of their potential applications in energy storage and conversion [30-33], magnetic [34], catalytic [35], and sensors [36] fields. However, oriented assembly of nanoscale building blocks is generally difficult and usually requires templates or substrates to control the direct growth. These preparation methods require sophisticated and expensive equipment, and also there are some limitations in controlling the size and shape of mesoporous materials. Therefore, exploration of a simple and economical approach is strongly desirable for the fabrication of porous nanostructures. Self-assembly is probably one of the simplest synthetic routes to synthesize nanostructures [29]. It is an important research subject to develop simple and reliable synthetic methods for hierarchically self-assembled architectures with designed crystallographic structure and controlled morphology, which strongly influence the properties of nanomaterials [29].

In this work, the synthesis of porous flower-like  $\alpha\text{-Fe}_2\text{O}_3$  nanostructures through iron alkoxide precursor and subsequent calcination at 200-700 °C is carried out. The samples prepared at different temperatures possess porosity resulting in high discharge capacity, good rate capability as well as cycling stability.

## 2. Experimental

The iron alkoxide precursor was prepared using ethylene glycol (EG, Merck) as reported elsewhere [13, 29]. In a typical synthesis,  $\text{FeCl}_3 \cdot 6\text{H}_2\text{O}$  (4.4 mmol SD Fine Chemicals), urea (90 mmol, Ranbaxy Laboratories), and tetrabutylammonium bromide (124 mmol, TBAB, Spectrochem) were added to 180 ml of EG in a 250 mL round bottomed flask.

The mixture was stirred for 10 min to obtain a homogeneous solution. The solution was refluxed at 195 °C for 30 min and a green precipitate of iron alkoxide was formed. The solution was cooled to room temperature normally, the precipitate was collected by centrifugation, washed with ethanol repeatedly and dried in an oven at 60 °C for 12 h. The iron alkoxide precursor samples were heated for 3 h at different temperatures between 200 and 700 °C in air. Red coloured powder samples were obtained. The schematic diagram of synthesis process is presented in Fig. 1.

Powder X-ray diffraction (XRD) patterns were recorded using Philips X-pertpro diffractometer at 40 kV and 30 mA using Cu K $\alpha$  ( $\lambda = 1.5418 \text{ \AA}$ ) radiation source. The morphology was examined using a Gemini Technology scanning electron microscopy (SEM) model ULTRA 55, and JEOL Co. transmission electron microscopy (TEM) model JEOL-JEM 2100F). Nitrogen adsorption/desorption isotherms were recorded by using Micromeritics surface area analyzer model ASAP 2020. The surface area was calculated using Brunauer-Emmett-Teller (BET) method in the relative pressure ( $p/p_0$ ) range 0.05-0.25 from adsorption branch of the isotherm. The pore size distribution was calculated by Barrett-Joyner-Halenda (BJH) method from the desorption branch. Thermogravimetric analysis (TGA) was recorded from ambient temperature to 800 °C at a heating rate of 10 °C min<sup>-1</sup> under flow of O<sub>2</sub> gas using NETZSCH thermal analyzer model TG 209 FI. Carbon and hydrogen elemental analyses were carried out using CHNS/O model Thermo Scientific Flash 2000 Organic Elemental Analyzer.

All electrochemical studies were carried out in a coin cells. For the fabrication of electrodes, the active material ( $\alpha$ -Fe<sub>2</sub>O<sub>3</sub>, 70 wt%), conductive material (Ketjen black, 20 wt%) and polyvinylidene fluoride (PVDF, 10 wt%, Aldrich) were mixed and ground in a mortar. Few drops of n-methyl pyrrolidinone (NMP, Aldrich) were added to form slurry. A copper disk (16 mm diameter) was polished with successive grades of emery, degreased,

etched in dilute 30%  $\text{HNO}_3$ , washed with detergent and rinsed with distilled water and acetone followed by drying in air. The slurry was coated on the pre-treated copper disk and dried at 110 °C under reduced pressure for 12 h. Coating and drying steps were repeated to get the mass of active material 2-5  $\text{mg cm}^{-2}$ . The electrodes were weighed using a Mettler Toledo electronic balance model AB265-S/FACT with sensitivity of 0.01 mg. Lithium metal foil (Aldrich) was used as the counter and reference electrode and Celgard porous propylene membrane (2400) was used as a separator. A commercial electrolyte of 1M  $\text{LiPF}_6$  in ethylene carbonate, diethyl carbonate and dimethyl carbonate (2:1:2 v/v) was used. Coin cells CR2032 (Hohsen corporation, Japan) were assembled in an argon filled glove box MBraun model UNILAB.

The cells were galvanostatically cycled in the potential range from 0.05 to 3.0 V at different current densities at room temperature. Cyclic voltammetry, galvanostatic charge-discharge cycling and rate capability experiments were carried out by using a Biologic SA multichannel potentiostat/galvanostat model VMP3.

### 3. Results and discussions

In the synthesis (Fig. 1) iron alkoxide is prepared by the addition of  $\text{FeCl}_3 \cdot 6\text{H}_2\text{O}$ , urea, TBAB to EG. When the solution was refluxed at 195 °C for 30 min, a green colour  $\text{Fe}^{+2}$  solution was formed by the reduction of  $\text{Fe}^{+3}$  ion by EG. The role of urea during the formation of the iron-EG complex was to supply  $\text{OH}^-$  ions by hydrolysis. The EG acted as both a ligand and a reducing agent. The reduction of  $\text{Fe}^{+3}$  by EG to form  $\text{Fe}^{+2}$  accompanies the release of HCl as a by-product. The released HCl was neutralized by  $\text{OH}^-$  ions from urea, this, facilitating the formation of a iron-EG complex [37]. The surfactant, TBAB was used as a structure directing reagent to control the flower-like architectures [29]. The complex of  $\text{Fe}^{2+}$ -EG undergoes nucleation and growth processes to form nanosheets, which in turn undergo self-assembly to form three-dimensional flower-like nanostructures [36, 38-40].

Figure 2 shows the TGA of the iron alkoxide precursor in air atmosphere. The weight loss is about 8 % up to 180 °C, due to the loss of adsorbed water. Subsequently 4% weight loss is observed up to 600 °C, which is attributed to the decomposition of organic part. Therefore iron alkoxide (S1) samples are heated at several temperatures from 200 to 700 °C for 3 h.  $\alpha$ -Fe<sub>2</sub>O<sub>3</sub> samples prepared at 200, 300, 400, 500, 600 and 700 °C are referred to as S2, S3, S4, S4, S5, S6 and S7, respectively.

The XRD patterns were used to examine the crystal structure of the precursor and Fe<sub>2</sub>O<sub>3</sub> samples (Fig. 3). The iron alkoxide precursor (Fig. 3a curve i) displays a strong diffraction peak at 11°, which agrees well with the reported pattern of iron alkoxide [29]. After heating of the precursor at temperature  $\geq$  200 °C, iron alkoxide is converted to iron oxide, but the product sample obtained at 200 °C exhibits a small impurity at 11° (Fig. 3a curve ii) which indicates that iron alkoxide is not totally converted to iron oxide at 200 °C. However, the XRD patterns ((Fig. 3b curve iii-vii) of samples heated at higher temperatures (S3, S4, S5, S6 and S7) agree well with the standard pattern for the rhombohedral structure of  $\alpha$ -Fe<sub>2</sub>O<sub>3</sub> (JCPDS 33-0664) with the lattice parameters,  $a = 5.036 \text{ \AA}$  and  $c = 13.748 \text{ \AA}$ . No crystalline impurities are detected, indicating that the products are pure and in single phase. In addition, the intense and sharp diffraction peaks suggest that the products have a high degree of crystallization. After decomposition of iron alkoxide, carbon may remain in the sample which cannot be detected by XRD. In order to examine the quantity of carbon and hydrogen, the samples were analyzed by CHNS/O analysis. The results indicated that the quantity of carbon is about 0.75, 0.22, 0.08 and 0.07% in S2, S4, S6 and S7, respectively, and the quantity of hydrogen is 0.22, 0.14, 0.07 and 0.06%.

The SEM images shown in Fig. 4 reveal a flower-like morphology for iron alkoxide precursor (Fig. 4a) as well as for all samples of  $\alpha$ -Fe<sub>2</sub>O<sub>3</sub> (Fig. 4b-g). The SEM images of lower magnification in Fig. 4b-g suggest that the samples are composed of numerous flowers

of diameter of 3-4  $\mu\text{m}$ . The magnified SEM images (Fig. 4 insets) show that each flower is composed of randomly assembled irregular-shaped nanosheets. It is interesting to observe that even after heating the alkoxide, the morphology of alkoxide precursor is retained by  $\text{Fe}_2\text{O}_3$  product samples. The microstructures of porous  $\alpha\text{-Fe}_2\text{O}_3$  are further characterized in detail by TEM. The low magnification TEM images (Fig. 5) also suggest that the samples maintain the flower-like morphology. It is interesting to observe porous structures on high magnification images (Fig. 5). There are innumerable pores of a few nanometer in size distributed on the surface of the petals, which are isolated from each other. The formation of the pores is likely due to the removal organic species from the iron alkoxide precursors during the heating process. Energy dispersive spectra show that the samples consist of Fe and O elements (Fig. 5g and 5h).

Xu et al., [37] proposed a mechanism for the formation of hierarchal nanostructured hollow microspheres assembled with nanosheets based on the Ostwald ripening process. In the reduction of  $\text{Fe}^{+3}$  by EG to form  $\text{Fe}^{+2}$ , EG molecule is coordinated with metal ions to form a metal-EG complex [37]. The Fe(II)-EG complex undergoes nucleation and growth processes to form nanosheets, which in turn undergo self-assembly to form three dimensional microspheres. According to Ostwald ripening process, the nanosheets located at the central core with a higher density will be dissolved and transferred to the outer shell with a lower density by a dissolution and recrystallization process, and in between a void space gradually forms in the core of the microsphere. This mechanism is schematically shown in Fig. 6 [36, 38-40].

To evaluate the porous nature of  $\alpha\text{-Fe}_2\text{O}_3$  nanostructures,  $\text{N}_2$  adsorption/desorption isotherms were recorded at  $-196^\circ\text{C}$ .  $\text{N}_2$  adsorption/desorption isotherms and BJH curves of  $\text{Fe}_2\text{O}_3$  samples are shown in Fig. 7. The isotherms correspond to type IV isotherms with hysteresis loops in the  $p/p_0$  range of 0.5-1.0 suggesting porous nature of the samples. The

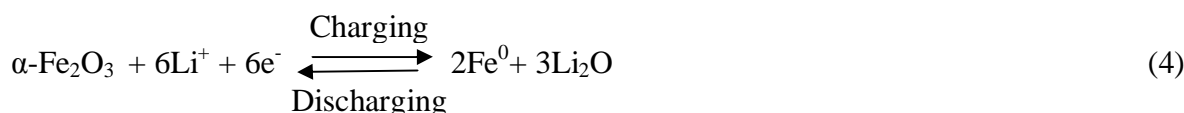
amount of N<sub>2</sub> adsorbed at  $p/p_0 = 0.995$  for S3, S4, S5, S6 and S7 samples are 144, 95, 64, 26 and 6 cm<sup>3</sup> g<sup>-1</sup> (Fig. 7a) and the corresponding surface area values are 53, 19, 15, 10 and 6 m<sup>2</sup> g<sup>-1</sup>. BJH curves also indicate the existence of porosity in all samples although the pore volume decreases by increasing the temperature of preparation (Table 1 and Fig. 7b). On increasing the preparation temperature, pore volume decreases and a broad distribution of pore diameter in the range of 2–100 nm is observed. The values of BET surface area, pore diameter and cumulative pore volume for all S3, S4, S5, S6 and S7 samples are listed in Table 1.

#### *Electrochemical studies:*

The electrochemical performance of electrodes made of  $\alpha$ -Fe<sub>2</sub>O<sub>3</sub> nanostructures was evaluated by cyclic voltammetry. Figure 7 shows the voltammograms of S3, S4 and S5 samples recorded at 0.05 mV s<sup>-1</sup> in the voltage range between 0.05 and 3.00 V. In the first cycle, three cathodic peaks (Ic, IIc and IIIc) are observed for all samples (Fig. 8) at about 1.55, 1.00 and 0.65 V, respectively, indicating the following three lithiation steps [7].



Thus, the overall reaction becomes:



At the initial stage of lithium intercalation (peak Ic), a small amount of Li is inserted into the crystal structure of the  $\alpha$ -Fe<sub>2</sub>O<sub>3</sub> without any change in the structure. In the second step of (peak IIc), the  $\alpha$ -Fe<sub>2</sub>O<sub>3</sub> is transformed to Li<sub>2</sub>Fe<sub>2</sub>O<sub>3</sub>. The high intensity peak (peak IIIc) corresponds to the complete reduction of Li<sub>2</sub>Fe<sub>2</sub>O<sub>3</sub>. In the anodic part of the voltammogram,

two broad overlapping peaks (Ia and IIa) are observed at 1.5 V and 2.06 V, which correspond to the oxidation Fe(0) to Fe(II) and further oxidation of Fe(II) to Fe(III), respectively. In the subsequent cycle, the cathodic peak of 1.56 V is different from that of the first cycle. A new cathodic peak appears at 0.8 V with low intensity, while the anodic polarization only showed broad peaks. The difference in the first and second cathodic curves is due to irreversible phase transformation in the initial cycle.

The charge/discharge curves of all  $\alpha$ -Fe<sub>2</sub>O<sub>3</sub> samples are shown in Fig. 9 in the voltage range between 0.05 and 3.00 V at specific current of 50 mA g<sup>-1</sup>. During first charging process from open circuit voltage to 0.05 V, Li<sup>+</sup> ions are inserted into the electrode material. During this process, three plateau regions are observed (Fig. 9 insets) in the voltage ranges from 1.7 to 1.50 V, 1.25 to 1.00 V and 0.90 to 0.50 V, respectively. The plateau regions correspond to the three processes (reactions 1-3), which are in agreement with the cyclic voltammograms (Fig. 8). The charge capacity of S3 sample in the first cycle is 1700 mAh g<sup>-1</sup>, whereas the discharge capacity is 1050 mAh g<sup>-1</sup>. Thus the cycling efficiency of the first cycle is only about 62%. In the second cycle, however, the values of charge and discharge capacities are 1100 and 1050 mAh g<sup>-1</sup>, respectively. The cycling efficiency thus improves in the second and subsequent cycles and comes close to 100%. The irreversible capacity loss of 650 mAh g<sup>-1</sup> noticed between the first and second cycles is attributed to phase stabilization of  $\alpha$ -Fe<sub>2</sub>O<sub>3</sub>. Similar observations are made from the charge/discharge cycling of the other  $\alpha$ -Fe<sub>2</sub>O<sub>3</sub> samples. The values of capacity, irreversible capacity loss and the efficiency of cycling are listed in Table 2. It is observed that the cycling performance of  $\alpha$ -Fe<sub>2</sub>O<sub>3</sub> sample prepared at 600 °C is superior to the rest of samples. The nature of cyclic voltammograms (Fig. 8) with large potential separations between anodic and cathodic peaks, as well as the charge/discharge voltage profiles (Fig. 9) with a large hysteresis between the charge and discharge plateaus is similar to the data reported on  $\alpha$ -Fe<sub>2</sub>O<sub>3</sub> as the anode material [7]. These

feature indicated slow kinetics of electron-transfer reactions, which appear to be inherent to the material.

The cycling stability of S3, S4, S5, S6 and S7 samples were tested by subjecting galvanostatic charge-discharge cycling at a specific current density of  $50 \text{ mA g}^{-1}$  in the voltage range between 0.05 and 3.00 V for 25 cycles. The cycle life data is shown in Fig. 10. For sample S3, a discharge capacity values of  $1058 \text{ mAh g}^{-1}$  and at the 25<sup>th</sup> cycle  $874 \text{ mAh g}^{-1}$  at the 25<sup>th</sup> cycle are obtained. Even though surface area decreased with an increase in the preparation temperature of samples (Fig. 7 and Table 1), the electrochemical performance increased due to an appropriate crystallinity of the sample. However, the sample S7 delivers lower capacity than the other samples due to very low surface area and pore volume. Samples S4, S5, S6 and S7 deliver an initial capacity values of 1407, 1236, 1156 and  $1132 \text{ mAh g}^{-1}$ , and the values at the 25<sup>th</sup> cycles are 795, 897, 1069 and  $783 \text{ mAh g}^{-1}$ , respectively. Thus, it is inferred that the  $\alpha\text{-Fe}_2\text{O}_3$  sample prepared at  $600 \text{ }^\circ\text{C}$  performs better due to an optimum crystallinity and surface area and porosity.

In order to study the rate capability,  $\alpha\text{-Fe}_2\text{O}_3$  samples (S3, S4, S5, S6 and S7) were subjected to charge/discharge cycling at different specific currents in the range from 95 to  $958 \text{ mA g}^{-1}$  (Fig. 11). On increasing the specific current from 95 to  $956 \text{ mA g}^{-1}$ , the discharge specific capacity values decrease from 1091, 1093, 967, 922 and  $722 \text{ mAh g}^{-1}$  to 103, 166, 250, 180 and  $170 \text{ mAh g}^{-1}$  for S3, S4, S5, S6 and S7 respectively. S5 sample exhibits better rate performance than the other samples, due to the suitable surface area and porosity.

Galvanostatic intermittent titration technique (GITT) was employed to determine the diffusion coefficient of  $\text{Li}^+$ -ion ( $D_{\text{Li}^+}$ ) into the S3 samples [41]. Before conducting GITT experiment, the cell was subjected to a charge/discharge cycle and the GITT experiment was conducted after 4 h of rest to reach equilibrium potential ( $E_0$ ). The electrode was subjected to lithiation by charging with a constant current ( $I$ ) for a time  $\tau$  so that the potential reached  $E_r$ .

Following this, charging was terminated and electrode was allowed to relax to reach open circuit steady-state potential  $E_s$ . From the values of  $\Delta E_\tau = (E_\tau - E_0)$  and  $\Delta E_s = (E_s - E_0)$ , the diffusion coefficient  $D_{Li^+}$  was calculated by using Eq. 5.

$$D_{Li^+} = (4/\pi\tau) (m_B V_m / M_B A)^2 (\Delta E_s / \Delta E_\tau)^2 \quad (5)$$

where  $m_B$  is the mass of the active material,  $M_B$  is the molar mass,  $V_m$  is molar volume and  $A$  is the area of the electrode. Fig. 12a shows a typical voltage variation as a function of time for a current pulse of 5  $\mu$ A beginning at 1.09 V and Fig. 12b shows the linear variation of voltage with square root of time over the voltage region of 1.09-1.035 V. Typical experimental values are  $\tau = 1000$  s,  $V_m = 52$  cm<sup>3</sup> mol<sup>-1</sup>,  $M_b = 159.69$  g and  $m_B = 1.725$  mg cm<sup>-2</sup>. The diffusion coefficient values obtained is  $5.4 \times 10^{-12}$  cm<sup>2</sup> s<sup>-1</sup>. This value of  $D_{Li^+}$  is in good agreement with the reported values for  $\alpha$ -Fe<sub>2</sub>O<sub>3</sub> [42-44].

## Conclusions

Porous flower-like  $\alpha$ -Fe<sub>2</sub>O<sub>3</sub> nanostructures were prepared by ethylene glycol mediated self assembly process via iron alkoxide precursor at different temperatures. The  $\alpha$ -Fe<sub>2</sub>O<sub>3</sub> samples were studied as anode materials for Li-ion battery. The first discharge capacity values were 1063, 1168, 1183, 1152 and 968 mAh g<sup>-1</sup> at a specific current of 50 mA g<sup>-1</sup> for  $\alpha$ -Fe<sub>2</sub>O<sub>3</sub> samples prepared at 300, 400, 500, 600 and 700 °C, respectively. There was no change in the morphology on heating to high temperatures. There is an increase in the crystallinity with concomitant decrease in surface area on increasing the preparation temperature. The results indicated that these  $\alpha$ -Fe<sub>2</sub>O<sub>3</sub> nanostructures have high reversible capacity, good capacity retention, and adequate rate capability, which makes them potential candidates for lithium ion batteries.

## Acknowledgements

SS and TRP acknowledge the financial support from the University Grant Commission (UGC), Government of India, under Dr. D.S. Kothari fellowship programme [Ref. No.F. 4-2/2006(BSR)/13-626/2012(BSR)] and senior research fellowship, respectively.

## References

1. T. Nagaura, K. Tozawa, Lithium ion rechargeable battery, *Prog. Battery and Solar Cells*, 9 (1990) 209.
2. L. Ji, Z. Lin, M. Alcoutlabi, X. Zhang, Recent developments in nanostructured anode materials for rechargeable lithium-ion batteries, *Energy Environ. Sci.*, 4 (2011) 2682.
3. J. Lee, M. C. Orilall, S. C. Warren, M. Kamperman, F. J. DiSalvo, U. Wiesner, Direct access to thermally stable and highly crystalline mesoporous transition-metal oxides with uniform pores, *Nat. Mater.* 7 (2008) 222.
4. P. L. Taberna, S. Mitra, P. Poizot, P. Simon, J. M. Tarascon, High rate capabilities  $\text{Fe}_3\text{O}_4$ -based Cu nano-architected electrodes for lithium-ion battery applications, *Nat. Mater.* 5 (2006) 567.
5. C. Xu, J. Sun, L. Gao, Direct growth of monodisperse  $\text{SnO}_2$  nanorods on graphene as high capacity anode materials for lithium ion batteries, *J. Mater. Chem.* 22 (2012) 975.
6. P. Poizot, S. Laruelle, S. Grugeon, L. Dupont, J. M. Tarascon, Nano-sized transition-metal oxides as negative-electrode materials for lithium-ion batteries, *Nature* 407 (2000) 496.
7. M. V. Reddy, T. Yu, C. H. Sow, Z. X. Shen, C. T. Lim, G. V. Subba Rao, B. V. R. Chowdari,  $\alpha\text{-Fe}_2\text{O}_3$  nanoflakes as an anode material for Li-ion batteries, *Adv. Funct. Mater.* 17 (2007) 2792.
8. B. Sun, J. Horvat, H. S. Kim, W. S. Kim, J. Ahn, G. Wang, Synthesis of mesoporous  $\alpha\text{-Fe}_2\text{O}_3$  nanostructures for highly sensitive gas sensors and high capacity anode materials in lithium ion batteries, *J. Phys. Chem. C* 114 (2010) 18753.

9. Z. Wang, D. Luan, S. Madhavi, C. M. Li, X. Wen (David) Lou,  $\alpha$ -Fe<sub>2</sub>O<sub>3</sub> nanotubes with superior lithium storage capability, *Chem. Commun.* 47 (2011) 8061.
10. Y. M. Lin, P. R. Abel, A. Heller, C.B. Mullins,  $\alpha$ -Fe<sub>2</sub>O<sub>3</sub> nanorods as anode material for lithium ion batteries, *J. Phys. Chem. Lett.* 2 (2011) 2885.
11. D. Wang, Q. Wang, T. Wang, Controlled synthesis of mesoporous hematite nanostructures and their application as electrochemical capacitor electrodes, *Nanotechnology* 22 (2011) 135604.
12. K. Xie, J. Li, Y. Lai, W. Lu, Z. Zhang, Y. Liu, L. Zhou, H. Huang, Highly ordered iron oxide nanotube arrays as electrodes for electrochemical energy storage, *Electrochem. Commun.* 13 (2011) 657.
13. S. Shivakumara, T. R. Penki, N. Munichandraiah, Synthesis and characterization of porous flowerlike  $\alpha$ -Fe<sub>2</sub>O<sub>3</sub> nanostructures for supercapacitor application, *ECS Electrochem. Lett.* 2 (2013) A60.
14. G. Sun, B. Dong, M. Cao, B. Wei, C. Hu, Hierarchical dendrite-like magnetic materials of Fe<sub>3</sub>O<sub>4</sub>,  $\gamma$ -Fe<sub>2</sub>O<sub>3</sub>, and Fe with high performance of microwave absorption, *Chem. Mater.* 23 (2011) 1587.
15. C. Cui, Y. Du, T. Li, X. Zheng, X. Wang, X. Han, P. Xu, Synthesis of electromagnetic functionalized Fe<sub>3</sub>O<sub>4</sub> microspheres/polyaniline composites by two-step oxidative polymerization, *J. Phys. Chem. B* 116 (2012) 9523.
16. Q. Hao, S. Liu, X. Yin, Z. Du, M. Zhang, L. Li, Y. Wang, T. Wang, Q. Li, Flexible morphology-controlled synthesis of mesoporous hierarchical  $\alpha$ -Fe<sub>2</sub>O<sub>3</sub> architectures and their gas-sensing properties, *Cryst. Eng. Comm.* 13 (2011) 806.
17. Y. Wang, J. Cao, S. Wang, X. Guo, J. Zhang, H. Xia, S. Zhang, S. Wu, Facile synthesis of porous  $\alpha$ -Fe<sub>2</sub>O<sub>3</sub> nanorods and their application in ethanol sensors, *J. Phys Chem. C* 112 (2008) 17804.

18. M. Hermanek, R. Zboril, N. Medrik, J. Pechousek, C. Gregor, Catalytic efficiency of iron (III) oxides in decomposition of hydrogen peroxide: competition between the surface area and crystallinity of nanoparticles, *J. Am. Chem. Soc.* 129 (2007) 10929.
19. J. Chen, L. Xu, W. Li, X. L. Gou,  $\alpha$ -Fe<sub>2</sub>O<sub>3</sub> nanotubes in gas sensor and lithium ion battery applications, *Adv. Mater.* 17 (2005) 582.
20. Z. Y. Wang, Z. C. Wang, S. Madhavi, W. L. Xiong,  $\alpha$ -Fe<sub>2</sub>O<sub>3</sub> mediated growth and carbon nanocoating of ultrafine SnO<sub>2</sub> nanorods as anode materials for Li-ion batteries, *J. Mater. Chem.* 22 (2012) 2526.
21. D. Larcher, C. Masquelier, D. Bonnin, Y. Chabre, V. Masson, J. B. Leriche, J. M. Tarascon, Effect of particle size on lithium intercalation into  $\alpha$ -Fe<sub>2</sub>O<sub>3</sub>, *J. Electrochem. Soc.* 150 (2003) A133.
22. A. S. Arico, P. Bruce, B. Scrosati, J. M. Tarascon, W. V. Schalkwijk, Nanostructured materials for advanced energy conversion and storage devices, *Nat. Mater.* 4 (2005) 366.
23. P. G. Bruce, B. Scrosati, J. M. Tarascon, Nanomaterials for rechargeable lithium batteries, *Angew. Chem., Int. Ed.* 47 (2008) 2930.
24. X. Jia, J. Chen, J. Xu, Y. Shi, Y. Fan, M. Zheng, Q. Dong, Fe<sub>2</sub>O<sub>3</sub> xerogel used as the anode material for lithium ion batteries with excellent electrochemical performance, *Chem. Commun.* 48 (2012) 7410.
25. J. Jin, S. I. Ohkoshi, K. Hashimoto, Giant coercive field of nanometer sized iron oxide, *Adv. Mater.* 16 (2004) 48.
26. Z. Pu, M. Cao, J. Yang, K. Huang, C. Hu, Controlled synthesis and growth mechanism of hematite nanorhombhedra, nanorods and nanocubes, *Nanotechnology* 17 (2006) 799.
27. K. Woo, H. J. Lee, J. P. Ahn, Y. S. Park, Sol-Gel mediated synthesis of Fe<sub>2</sub>O<sub>3</sub> nanorods *Adv. Mater.* 15 (2003) 1761.
28. J. Chen, L. Xu, W. Li, X. Gou,  $\alpha$ -Fe<sub>2</sub>O<sub>3</sub> Nanotubes in gas sensor and lithium-ion battery

applications, *Adv. Mater.* 17 (2005) 582.

29. L. S. Zhong, J. S. Hu, H. P. Liang, A. M. Cao, W. G. Song, L. J. Wan, Self-assembled 3D flowerlike iron oxide nanostructures and their application in water treatment *Adv. Mater.* 18 (2006) 2426.

30. X. W. Lou, Y. Wang, C. Yuan, J. Y. Lee, L. A. Archer, Template-free synthesis of SnO<sub>2</sub> hollow nanostructures with high lithium storage capacity, *Adv. Mater.* 18 (2006) 2325.

31. S. H. Ko, D. Lee, H. W. Kang, K. H. Nam, J. Y. Yeo, S. J. Hong, C. P. Grigoropoulos, H. J. Sung, Nanoforest of Hydrothermally Grown Hierarchical ZnO Nanowires for a High Efficiency Dye-Sensitized Solar Cell, *Nano Lett.* 11 (2011) 666.

32. Y-J. Kim, J. Yoo, B-H. Kwon, Y. J. Hong, C-H. Lee, G-C. Yi, Position-controlled ZnO nanoflowers arrays grown on glass substrates for electron emitter application, *Nanotech.* 19 (2008) 315202.

33. C. Y. Jiang, X. W. Sun, G. Q. Lo, D. L. Kwong, Improved dye-sensitized solar cells with a ZnO-nanoflower photoanode, *Appl. Phys. Lett.* 90 (2007) 263501.

34. X. Liu, X. Duan, Q. Qin, Q. Wang, W. Zheng, Ionic liquid-assisted solvothermal synthesis of oriented self-assembled Fe<sub>3</sub>O<sub>4</sub> nanoparticles into monodisperse nanoflakes *Cryst. Eng. Comm.* 15 (2013) 3284.

35. K. Zhu, D. Wang, J. Liu, Self-assembled materials for catalysis, *Nano Research* 2 (2009) 129.

36. J. Chang, M. Z. Ahmad, W. Wlodarski, E. R. Waclawik, Self-assembled 3D ZnO porous structures with exposed reactive {0001} facets and their enhanced gas sensitivity, *Sensors* 13 (2013) 8445.

37. J. S. Xu, Y. J. Zhu,  $\alpha$ -Fe<sub>2</sub>O<sub>3</sub> hierarchically hollow microspheres self-assembled with nanosheets: surfactant-free solvothermal synthesis, magnetic and photocatalytic properties, *Cryst. Eng. Comm.* 13 (2011) 5162.

38. D. Larcher, G. Sudant, R. Patrice, J. M. Tarascon, Some Insights on the use of polyols-based metal alkoxides powders as precursors for tailored metal oxides particles, *Chem. Mater.* 15 (2003) 3543.
39. B. Liu, H. C. Zeng, Symmetric and asymmetric Ostwald ripening in the fabrication of homogeneous core-shell semiconductors, *small* 1 (2005) 566.
40. J. J. Zhang, Y. L. Chen, Y. F. Sun, T. Huang and A. S. Yu, Hierarchical hollow Fe<sub>2</sub>O<sub>3</sub> micro-flowers composed of porous nanosheets as high performance anodes for lithium-ion batteries, *RSC Adv.*, 3 (2013) 20639.
41. W. Weppner, R.A. Huggins, Determination of the kinetic parameters of mixed-conducting electrodes and application to the system L<sub>3</sub>Sb, *J. Electrochem. Soc.* 124 (1977) 1569.
42. M.G.S.R. Thomas, P. G. Bruce, J. B. Goodenough, AC Impedance analysis of polycrystalline insertion electrodes: application to Li<sub>1-x</sub>CoO<sub>2</sub>, *J. Electrochem. Soc.* 132 (1985) 1521.
43. D. Aurbach, M.D. Levi, and A. Schechter, *J. Electrochem. Soc.* Pennington, NJ, 124 (1997).
44. P. Suresh, A. K. Shukla, N. Munichandraiah, Temperature dependence studies of a.c. impedance of lithium-ion cells, *J. Appl. Electrochem.* 32 (2002) 267.

**Figure 1.** The schematic diagram of synthesis process

**Figure 2.** TGA curve of iron alkoxide sample (S1)

**Figure 3.** XRD patterns of samples (a) (i) S1, (ii) S2, and  $\alpha$ -Fe<sub>2</sub>O<sub>3</sub> samples (b), (iii) S3, (iv) S4 (v) S5, (vi) S6 and (vii) S7

**Figure 4.** SEM images of samples: (a) S1, (b) S2, (c) S3, (d) S4, (e) S5, (f) S6 and (g) S7 with higher magnification images in insets.

**Figure 5.** TEM images of porous  $\alpha$ -Fe<sub>2</sub>O<sub>3</sub> samples: (a) S1, (b) S3, (c) S4, (d) S5, (e) S6 and (f) S7 3) and EDS patterns of (g) S1 and (h) S6.

**Figure 6.** Schematic mechanism for the formation of flower-like  $\alpha$ -Fe<sub>2</sub>O<sub>3</sub> nanostructures

**Figure 7.** (a) BET isotherms of porous  $\alpha$ -Fe<sub>2</sub>O<sub>3</sub> samples: (i) S3, (ii) S4, (iii) S5, (iv) S6 and (v) S7. (b) BJH pore-size distribution of porous  $\alpha$ -Fe<sub>2</sub>O<sub>3</sub> samples. S7 sample isotherm and BJH are shown in inset of A and B. curves (iv), (iii), (ii) and (i) are, respectively, vertically shifted by 10, 15, 20 and 25 units of Y-axis scale relative to the position of curve (v).

**Figure 8.** Cyclic voltammograms of  $\alpha$ -Fe<sub>2</sub>O<sub>3</sub> samples: (a) S3, (b) S4 and (c) S5 at a sweep rate of 0.05 mV s<sup>-1</sup> in the potential range of 0.01-3.0 V. I<sub>c</sub>, I<sub>2c</sub> and I<sub>3c</sub> are cathodic peaks, I<sub>a</sub> and I<sub>2a</sub> are anodic peaks and 1, 2, 3 and 4 are indicating the cycle number. Electrode area = 1.1 cm<sup>2</sup> and active material loading = 2.5-3.0 mg cm<sup>-2</sup>.

**Figure 9.** Charge-discharge curves at a specific current of 50 mA g<sup>-1</sup> for  $\alpha$ -Fe<sub>2</sub>O<sub>3</sub> samples: (a) S3, (b) S4, (c) S5, (d) S6 and (e) S7. Electrode area = 2.0 cm<sup>2</sup> and active material loading = 2 ~ 3.0 mg cm<sup>-2</sup>.

**Figure 10.** Electrochemical cyclability test of  $\alpha$ -Fe<sub>2</sub>O<sub>3</sub> samples: (i) S3, (ii) S4, (iii) S5, (iv) S6 and (v) S7 at a specific current of 50 mA g<sup>-1</sup> and (vi) coulombic efficiency S6. Electrode area = 2.0 cm<sup>2</sup> and active material loading 2 ~ 3.0 mg cm<sup>-2</sup>.

**Figure 11.** Discharge specific capacity of  $\alpha$ -Fe<sub>2</sub>O<sub>3</sub> samples: (i) S3, (ii) S4, (iii) S5, (iv) S6 and (v) S7. Electrode area = 2.0 cm<sup>2</sup> and active material loading = ~2-3.0 mg cm<sup>-2</sup>. Specific currents used for charge/discharge cycling are indicated in mA g<sup>-1</sup>.

**Figure 12.** (a) Galvanostatic intermittent titration technique (GITT) curve of S3 sample and (b) variation of cell potential against  $\tau^{1/2}$  to show the linear fit.

**Table 1.** N<sub>2</sub> adsorption/desorption data of  $\alpha$ -Fe<sub>2</sub>O<sub>3</sub> samples.

S.No	samples	BET surface area (m <sup>2</sup> g <sup>-1</sup> )	Pore diameter (nm)	Average pore diameter (nm)
1	S3	53	6.5	19.6
2	S4	19	20.6	24.3
3	S5	15	46.1	46.3
4	S6	10	51.3	47.7
5	S7	6	19.2	30.2

**Table 2.** The first two cycles charge/discharge capacity values with coulombic efficiency at a specific current of 50 mA g<sup>-1</sup> for all  $\alpha$ -Fe<sub>2</sub>O<sub>3</sub> samples.

sample	Capacities of 1 <sup>st</sup> cycle		Efficiency %	Capacities of 2 <sup>nd</sup> cycle		Efficiency %
	charge	discharge		charge	discharge	
S3	1703	1058	62	1116	1043	93
S4	1485	1236	83	1053	1057	100
S5	1761	1240	70	1284	1221	95
S6	1719	1156	67	1160	1165	100
S7	1818	1132	62	1174	1107	94

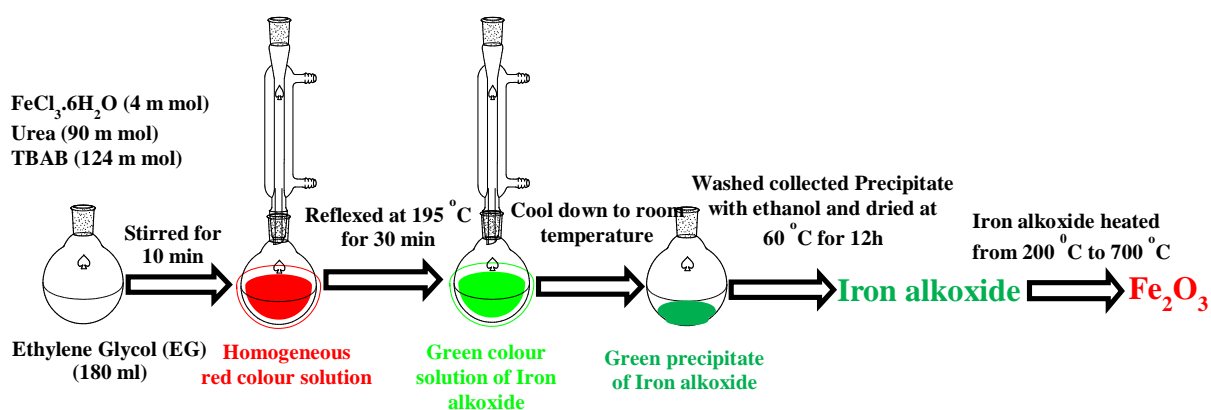


Figure 1

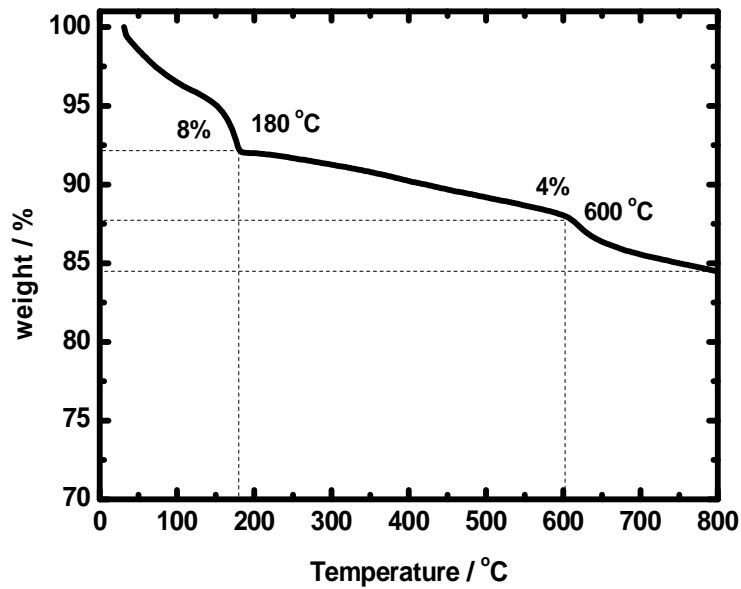


Figure 2

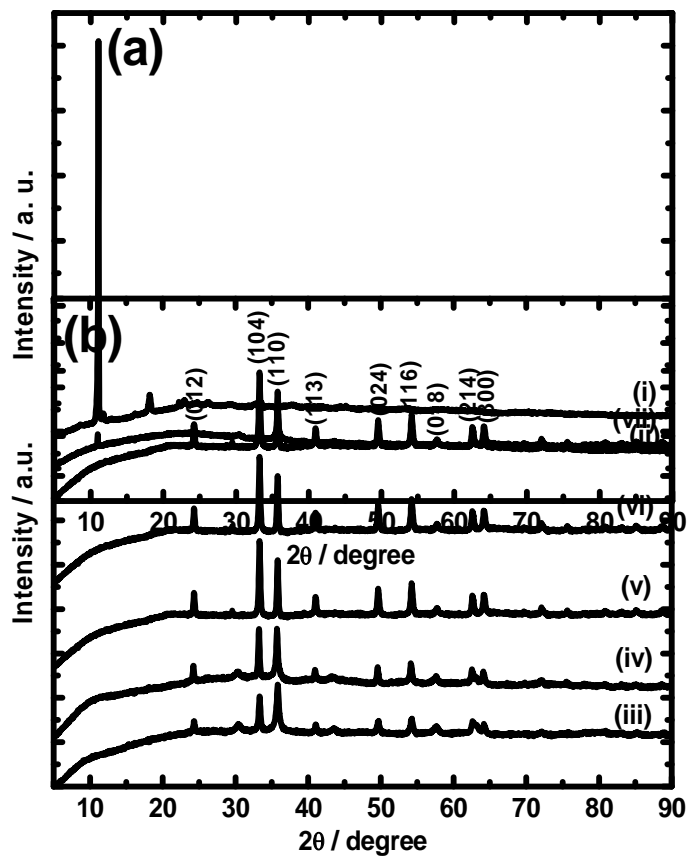


Figure 3

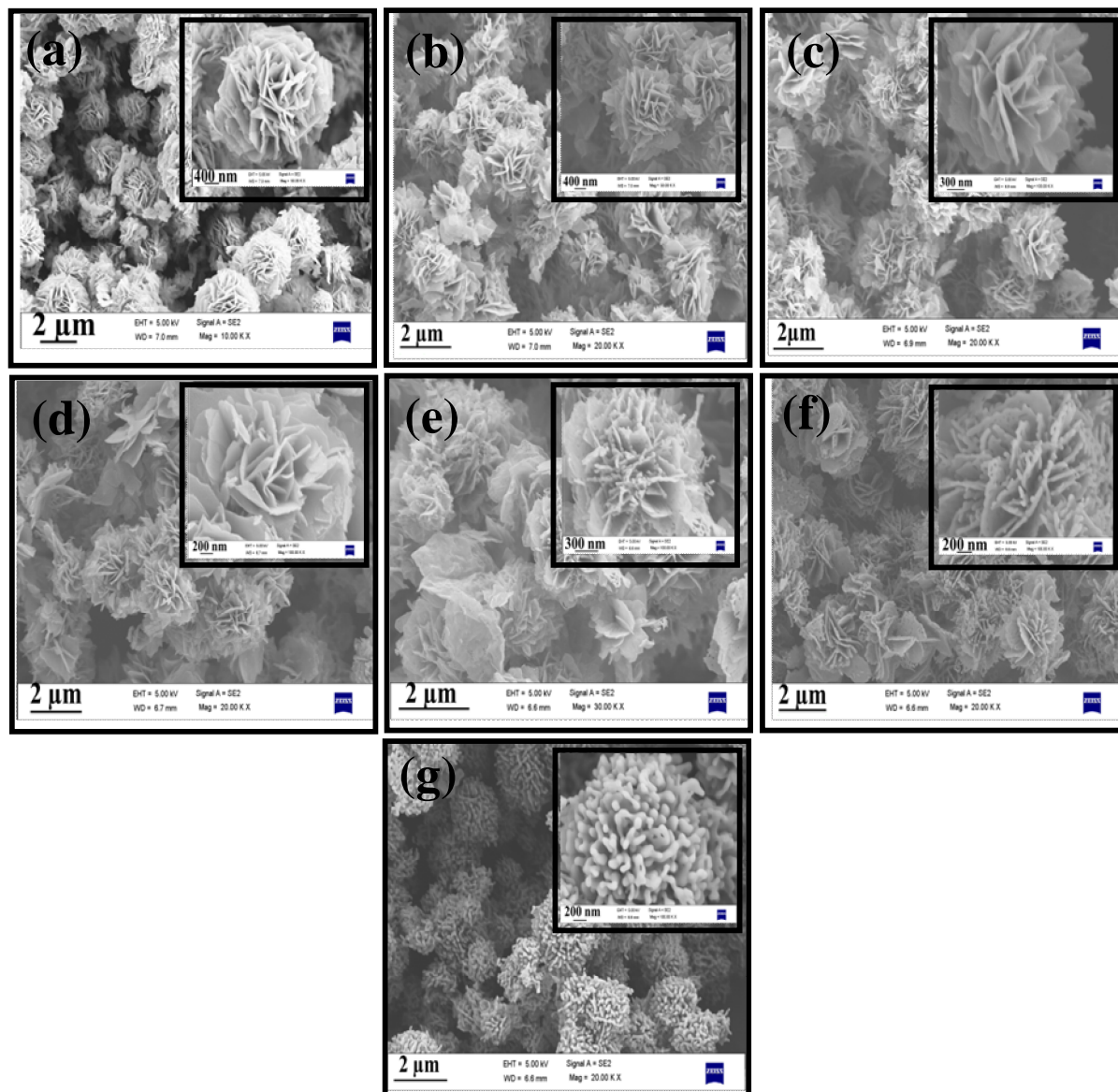


Figure 4

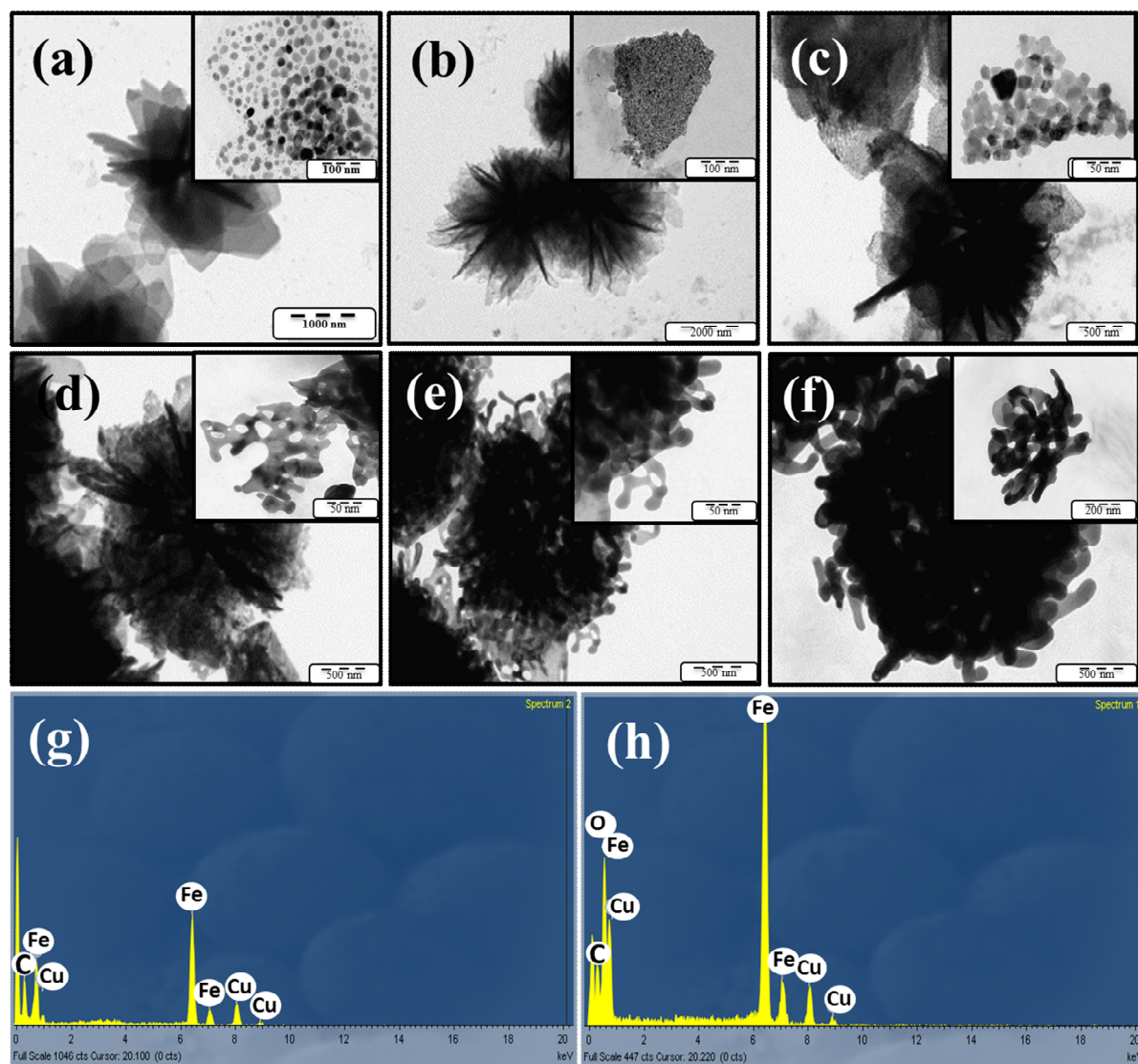


Figure 5

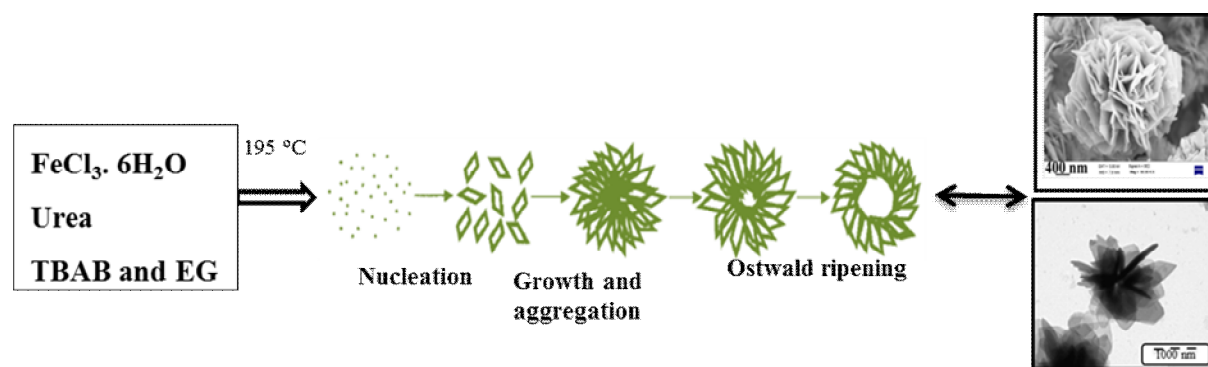


Figure 6

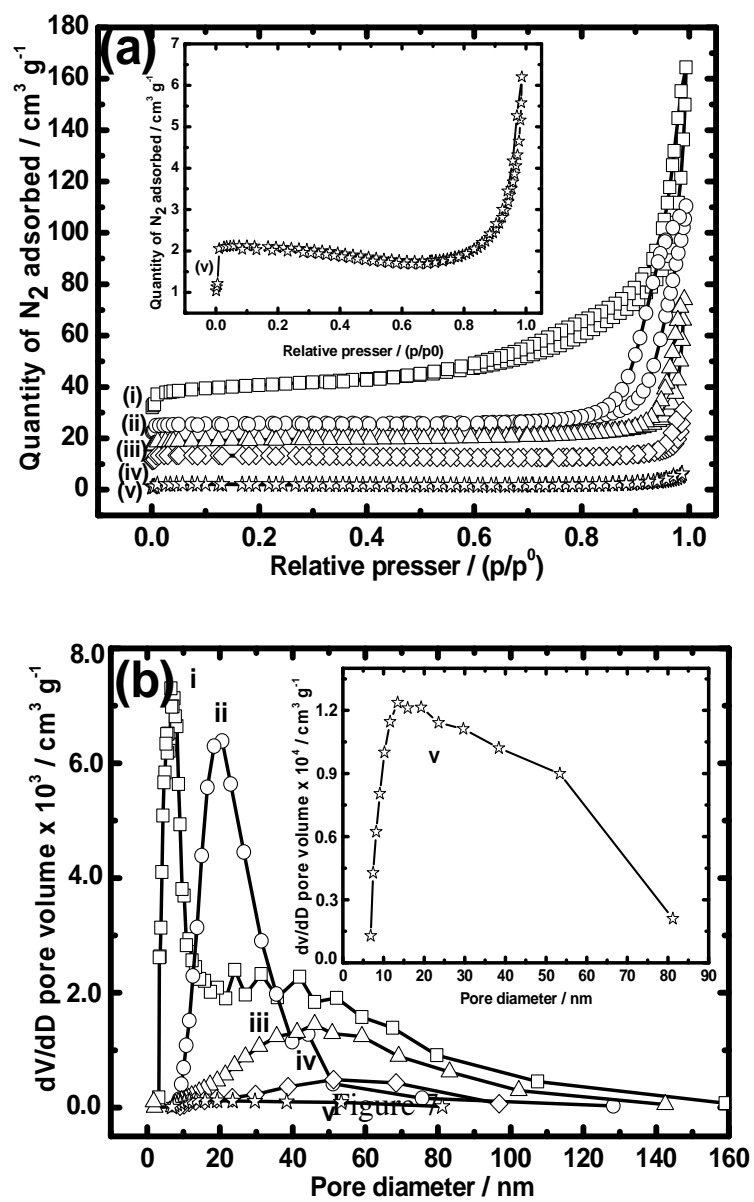


Figure 7

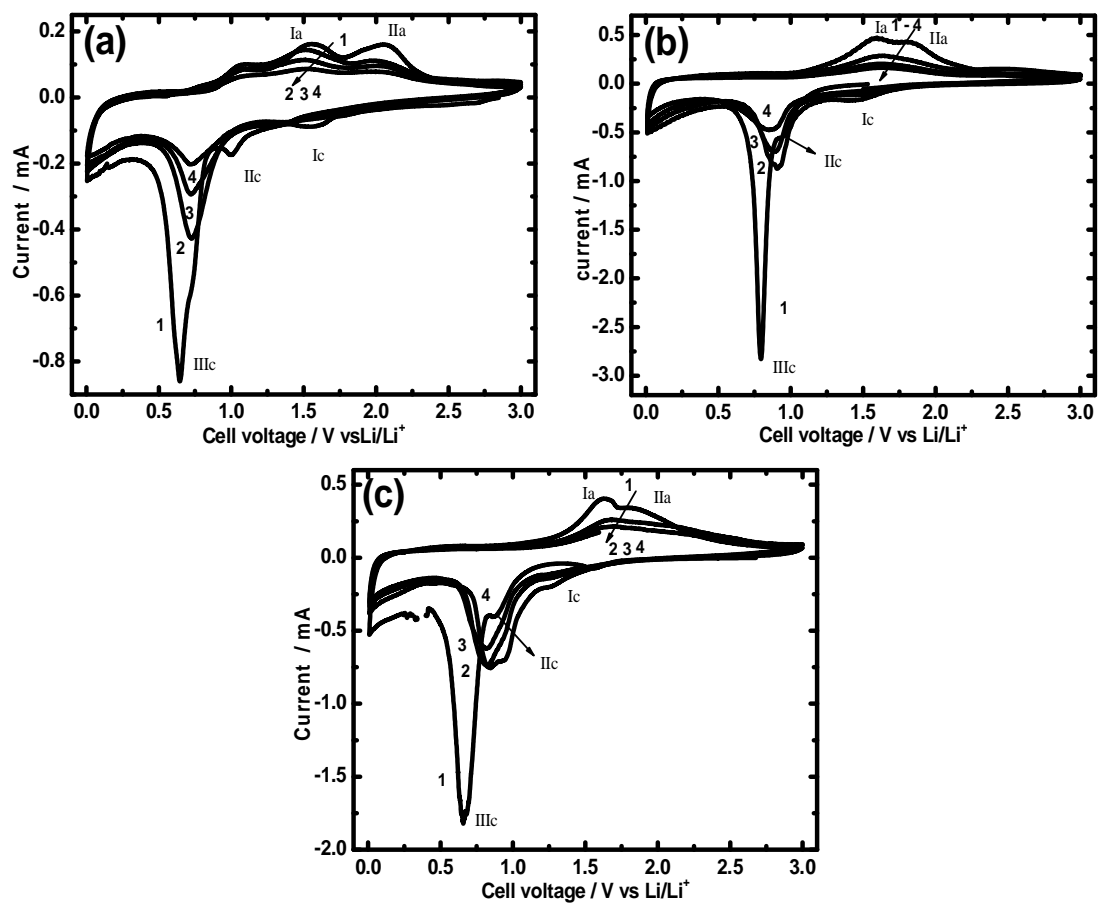


Figure 8

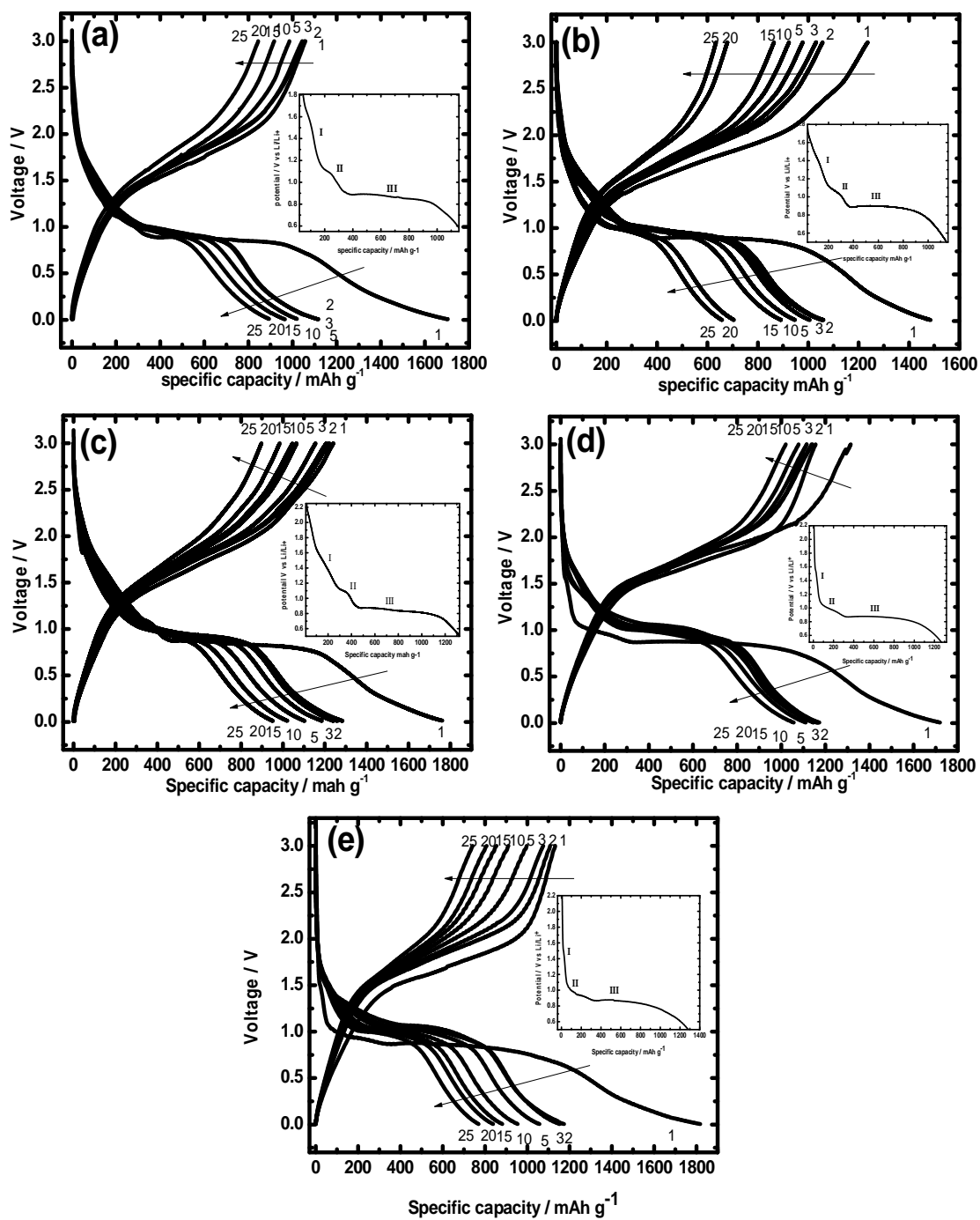


Figure 9

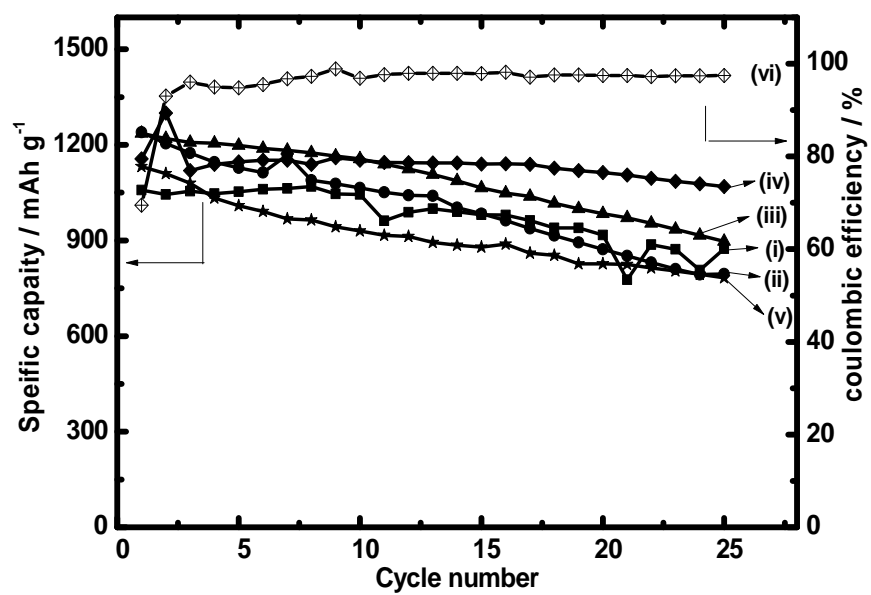


Figure 10

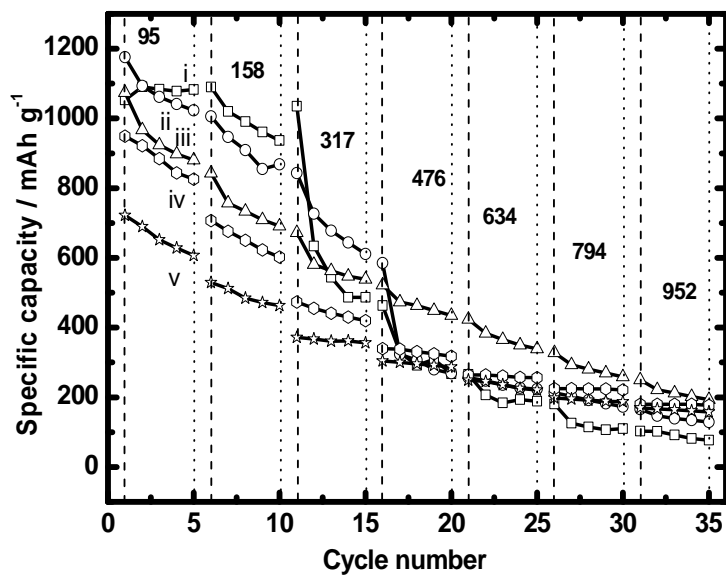


Figure 11

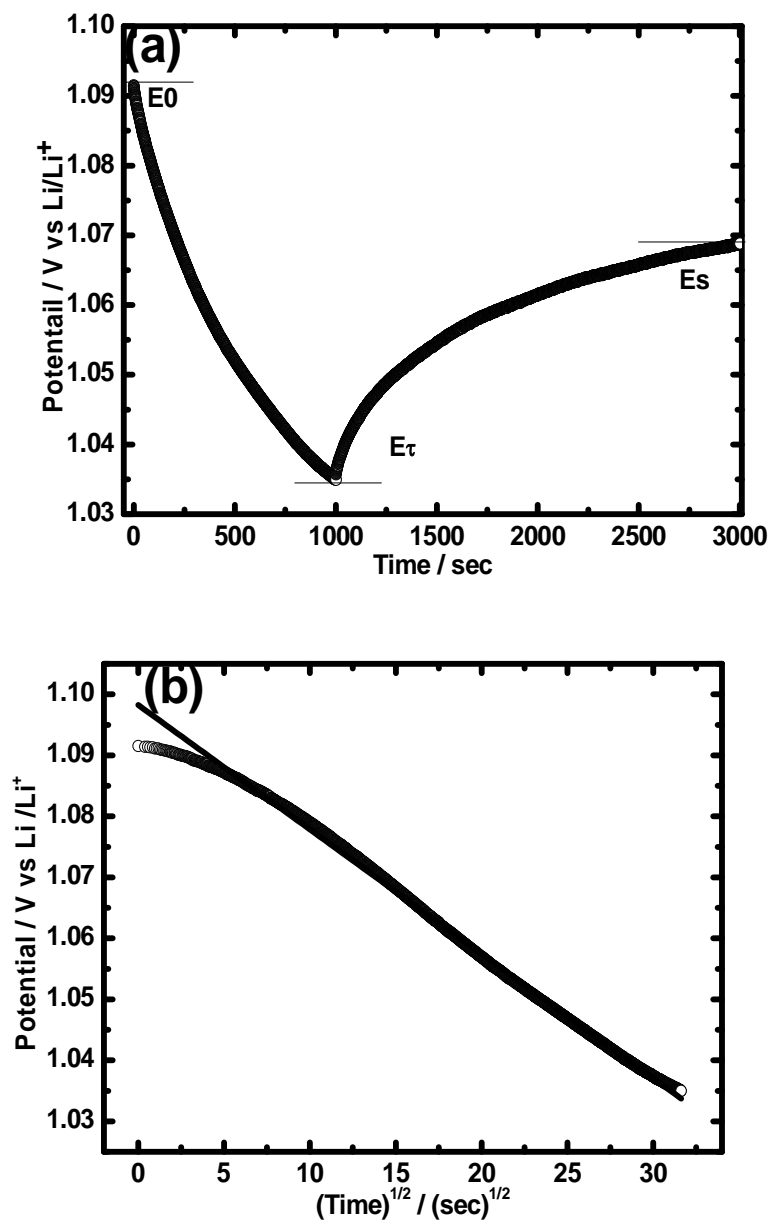


Figure 12